

Manifold lifting: scaling MCMC to the vanishing noise regime

Khai Xiang Au (khai@u.nus.edu)¹, Matthew M. Graham (m.m.graham@nus.edu.sg)², and
Alexandre H. Thiery (a.h.thiery@nus.edu.sg)²

¹*Graduate School for Integrative Sciences and Engineering, National University of Singapore*
²*Department of Statistics and Applied Probability, National University of Singapore*

Abstract

Standard Markov chain Monte Carlo methods struggle to explore distributions that are concentrated in the neighbourhood of low-dimensional structures. These pathologies naturally occur in a number of situations. For example, they are common to Bayesian inverse problem modelling and Bayesian neural networks, when observational data are highly informative, or when a subset of the statistical parameters of interest are non-identifiable. In this paper, we propose a strategy that transforms the original sampling problem into the task of exploring a distribution supported on a manifold embedded in a higher dimensional space; in contrast to the original posterior this lifted distribution remains diffuse in the vanishing noise limit. We employ a constrained Hamiltonian Monte Carlo method which exploits the manifold geometry of this lifted distribution, to perform efficient approximate inference. We demonstrate in several numerical experiments that, contrarily to competing approaches, the sampling efficiency of our proposed methodology does not degenerate as the target distribution to be explored concentrates near low dimensional structures.

1 Introduction

Under a Bayesian framework, inference corresponds to deducing the posterior distribution on unknown variables given an observation model and a prior distribution. While we generally expect conditioning on observed data to reduce the uncertainty about the possible values of the unknown variables, in most real-world situations we also expect to retain some uncertainty in our posterior beliefs. Accurately quantifying this uncertainty is important in downstream tasks such as using a model to make predictions or comparing how well competing models explain the observed data.

An obvious source of uncertainty in our posterior beliefs is observation noise, where observations are imperfectly measured due to, for instance, instrument limitations or human error. Uncertainty also naturally arises in ill-posed or underdetermined problems, that is when the number of degrees of freedom in the unknown variables exceeds the number of degrees of freedom constrained by the observations. Even in the case of plentiful noiseless observations, uncertainty may still arise due to inherent non-identifiabilities in the model.

In this paper, we consider inference in models where we have noisy and non-linear *observations* $y \in \mathcal{Y} \equiv \mathbb{R}^{d_y}$ of an unknown *quantity of interest* $\theta \in \Theta \equiv \mathbb{R}^{d_\theta}$. Although the methodology we describe can be applied more generally, for conceptual clarity, we focus on the case where the observation noise is additive, isotropic and Gaussian. The observation model is then defined as

$$y = F(\theta) + \sigma\eta \quad (1)$$

for a Gaussian *noise variable* $\eta \sim \mathcal{N}(0, \mathbf{I}_{d_y})$, *noise intensity* $\sigma > 0$ and *forward operator* $F : \Theta \rightarrow \mathcal{Y}$. The mapping F is typically non-linear and computationally expensive to evaluate. We adopt the Bayesian framework and specify a prior distribution on Θ with unnormalised density $\exp[-\Phi_0(\theta)]$ with respect to the Lebesgue measure. The negative logarithm of the posterior density $\pi^\sigma : \Theta \rightarrow \mathbb{R}_{\geq 0}$ then reads

$$-\log \pi^\sigma(\theta) = \Phi_0(\theta) + \frac{1}{2\sigma^2} \|y - F(\theta)\|^2 + \text{constant}. \quad (2)$$

In the case where the forward operator F is linear and the prior distribution Gaussian, the posterior distribution is also Gaussian. In general, though, the posterior distribution is not tractable and approximate inference methods are necessary to explore the posterior distribution. There are natural situations where the dimensionality of the observations is lower, and often much lower, than the dimensionality of the quantity of interest. In these settings, i.e. $d_Y < d_\Theta$, even as the noise intensity σ decreases to zero, exact reconstruction of the quantity of interest is typically not possible: the system is underdetermined. In *Bayesian inverse problems* [Stu10, KvdVvZ11, PMSG14], a particularly representative class of models where this type of scenario naturally occurs, the quantity of interest θ typically represents a spatially extended field. The forward operator F describes the process of collecting a (typically small) set of measurements derived from θ . For example, in Section 5.3 we consider the problem of reconstructing a thermal conductivity field from a discrete set of noisy measurements of a temperature field; the temperature field is obtained from the conductivity field as the solution to an elliptic *partial differential equation* (PDE).

Conversely, even when there are plentiful observations when compared to the number of unknowns, i.e. $d_Y \gg d_\Theta$, structural non-identifiabilities in the observation model formulation — that multiple values of θ give the same conditional distribution on observations y — can mean that as the observation noise vanishes ($\sigma \rightarrow 0$), the posterior distribution on θ also does not collapse to a point. As an example, in Section 5.2 we consider the problem of inferring the parameters θ of a simple *ordinary differential equation* (ODE) model of neuronal dynamics given a sequence of noisy observations. The natural parametrisation of this model is such that a subset of parameters are non-identifiable. In this model, and in other simple cases, reparametrisations may allow non-identifiabilities to be removed. In more complex models, however, it may not be tractable to find such a parametrisation, or even know prior to performing inference that non-identifiabilities are present.

Although in above-mentioned cases it is not possible to exactly reconstruct the quantity of interest as the observation noise vanishes $\sigma \rightarrow 0$, the posterior distribution will concentrate on a subset $\mathcal{S} \subset \Theta$ of the latent space given by

$$\mathcal{S} = \{\theta \in \Theta : F(\theta) = y\}.$$

Under mild regularity assumptions on the forward operator F , the subset \mathcal{S} is a submanifold of dimension $d_{\mathcal{S}} = d_\Theta - d_Y$ embedded in Θ and the bulk of the posterior mass is distributed in a neighbourhood of radius $\mathcal{O}(\sigma)$ around \mathcal{S} .

The key computation involving the posterior distribution in downstream tasks is the evaluation of posterior expectations of the form $\int_\Theta \varphi(\theta) \pi^\sigma(\theta) d\theta$ for a test function $\varphi : \Theta \rightarrow \mathbb{R}$. We focus in this text on *Markov chain Monte Carlo* (MCMC) methods for approximating such posterior expectations. We assume throughout that derivatives of the forward operator F and prior negative log-density Φ_0 can be computed and develop MCMC methods which exploit this derivative information.

Many of the most widely-used MCMC methods for general target distributions on \mathbb{R}^{d_Θ} such as *random-walk Metropolis* (RWM) with Gaussian proposals, the *Metropolis-adjusted Langevin algorithm* (MALA) [Bes94] and *Hamiltonian Monte Carlo* (HMC) [DKPR87], require the setting of a step size parameter which controls the scale of the proposed moves. The efficiency of these methods is highly dependent on an appropriate choice of this step size parameter, with too large steps leading to a high probability of proposed moves being rejected, while overly small steps leading to slow exploration.

In the past decades, much analysis has been done to identify optimal scaling of the step size of various MCMC algorithms as the target distribution dimension becomes large, i.e. the $d_\Theta \rightarrow \infty$ asymptotic [GIKP90, RGG97, RR01, BPR⁺13]. In contrast, comparably little attention has been devoted to the vanishing noise asymptotic, i.e. $\sigma \rightarrow 0$. As the posterior concentrates increasingly close to the manifold \mathcal{S} , this induces a strong anisotropy in the scaling of the posterior distribution in different directions, with large changes in posterior density in directions normal to \mathcal{S} and much smaller changes in direction tangential to \mathcal{S} . Importantly, for non-linear manifolds \mathcal{S} , the tangential and normal directions vary across the manifold so that a simple global rescaling will not be sufficient to counteract the anisotropy.

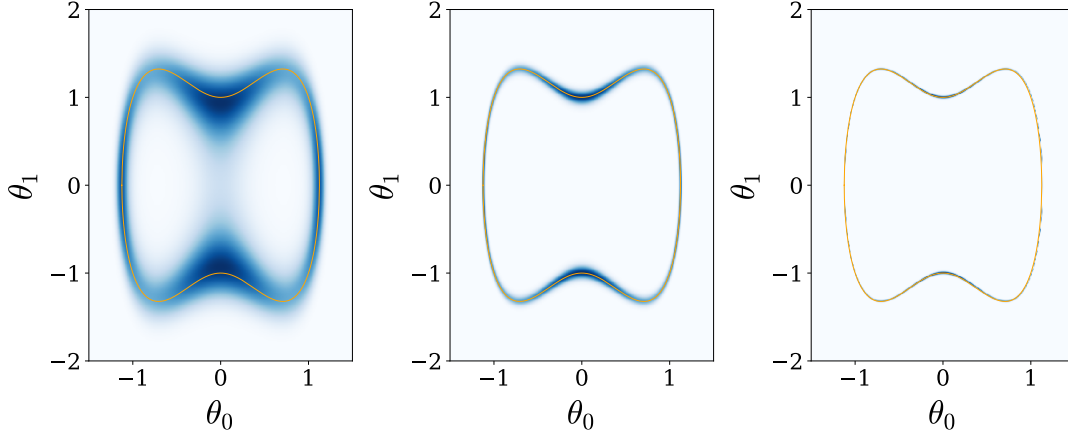


Figure 1: Posterior distribution for noise intensities $\sigma \in \{0.5, 0.1, 0.02\}$ (left-to-right) in toy example with forward operator $F(\theta) = \theta_1^2 + 3\theta_0^2(\theta_0^2 - 1)$. The blue heatmaps show the posterior density π^σ with darker colours indicating higher density. The orange curves show the limiting manifold \mathcal{S} .

In [B RTP18] the authors analyse the performance of RWM algorithms in this vanishing noise regime in the specific case where the manifold \mathcal{S} is a linear subspace of Θ . They prove that the step size needs to be scaled linearly with σ to avoid the acceptance probability to decrease to zero in the limit when $\sigma \rightarrow 0$. As we will describe in the following section, this limitation also applies to gradient-based MCMC methods such as MALA and HMC.

Although [B RTP18] concentrate on the linear case, they acknowledge that the more practically relevant case is of a non-linear limiting manifold \mathcal{S} , and state that an important area for future work is the ‘study of MCMC algorithms that better exploit the manifold structure of the support of the target distribution’ where the ‘manifold can be of smaller dimension than the general space’. The main contribution of this paper is precisely a practical methodology for this setting: we propose an MCMC algorithm which exploits the manifold structure of the target posterior distribution in order to remain computationally efficient in the vanishing noise regime.

The remainder of the paper is structured as follows. We begin in Section 2 by illustrating how standard MCMC methods breakdown in the limit of $\sigma \rightarrow 0$ in an illustrative two-dimensional example. In Section 3 we introduce an augmented state space formulation which lifts the target posterior distribution on to a manifold in a higher dimensional space, with this lifted target distribution not suffering the degenerate anisotropic scaling exhibited in the original space as $\sigma \rightarrow 0$. In Section 4 we describe our proposed approach of using a constrained HMC algorithm to generate samples according to this manifold-restricted lifted target distribution. Finally, in Section 5 we present the results of numerical experiments which empirically demonstrate that, in contrast to existing MCMC methods, the proposed methodology is robust to low observation noise.

2 Vanishing noise asymptotic regime

In this section we numerically illustrate in a toy example the behavior of standard MCMC methods in the vanishing noise asymptotic $\sigma \rightarrow 0$. Consider a model of the form defined in (1) with $d_\Theta = 2$ and $d_Y = 1$ and a forward operator $F : \mathbb{R}^2 \rightarrow \mathbb{R}$ given by

$$F(\theta) = \theta_1^2 + 3\theta_0^2(\theta_0^2 - 1). \quad (3)$$

We assume we observe $y = 1$ and place a standard centred Gaussian prior on the unknown parameter, i.e. $\theta \sim \mathcal{N}(0, \mathbf{I}_2)$. The posterior distribution is depicted in Figure 1 for three noise intensities $\sigma \in \{0.5, 0.1, 0.02\}$. As $\sigma \rightarrow 0$, the posterior distribution can be seen to concentrate in the neighbourhood of the manifold \mathcal{S} implicitly defined by the set of solutions to the equation $F(\theta) = y$.

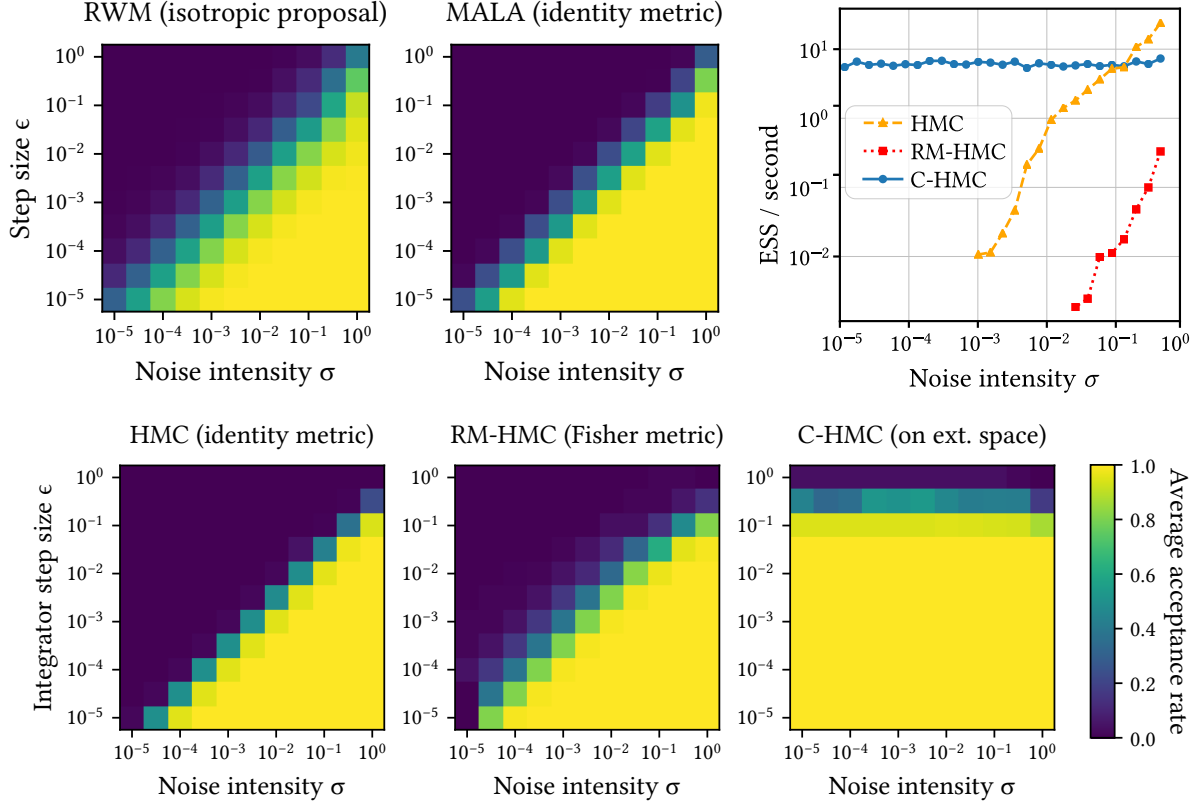


Figure 2: Heat maps: Average acceptance rate for chains simulated using different Metropolis MCMC methods targetting posterior π^σ of toy example for varying noise intensities σ and (integrator) step sizes ϵ . For the HMC methods $N = 10$ integrator steps were used per sample. The values displayed are means of the Metropolis accept probabilities over four chains of 200 (RWM and MALA) or 20 (HMC, RM-HMC and C-HMC) samples initialised at equispaced points around the limiting manifold \mathcal{S} . Top right: Sampling efficiency (effective sample size over chain run time in seconds) of HMC, RM-HMC and C-HMC. Contrarily to HMC and RM-HMC, the efficiency of C-HMC does not degrade as $\sigma \rightarrow 0$.

We consider first the performance of the RWM algorithm with isotropic Gaussian proposals with standard deviation (step size) $\epsilon > 0$. For the proposal to have a non-vanishing acceptance rate in this setting, the step size ϵ needs to be of order $\mathcal{O}(\sigma)$ (see top-left panel in Figure 2). As RWM chains evolve on a diffusive scale, we require $\mathcal{O}(\epsilon^{-2}) = \mathcal{O}(\sigma^{-2})$ steps to move a $\mathcal{O}(1)$ distance in Θ [BRT18]. To informally describe this phenomenon, we state that RWM degenerates at rate σ^{-2} as $\sigma \rightarrow 0$.

Maybe surprisingly, despite the use of gradient information, the performance of MALA chains is typically not better than RWM (see top-centre panel in Figure 2). Indeed, since in the neighbourhood of \mathcal{S} the gradient of the (logarithm of the) posterior density is approximately orthogonal to the tangent plane to \mathcal{S} , the gradient information by itself does not help MALA chains to explore the directions in the parameter space with greatest variation i.e. the directions that are tangential to \mathcal{S} . Further, as the exploration of the parameter space remains diffusive, MALA also degenerates at rate σ^{-2} .

HMC methods with a fixed metric (mass matrix) enjoy a slightly better scaling. In order to maintain a non-vanishing acceptance probability, the step size parameter $\epsilon > 0$ of the leapfrog integrator used to generate proposals, like the RWM step size, still needs to be chosen of order $\mathcal{O}(\sigma)$ to maintain a non-zero acceptance rate (see bottom-left panel in Figure 2). However for proposals generated by simulating $\mathcal{O}(\epsilon^{-1}) = \mathcal{O}(\sigma^{-1})$ such leapfrog steps, the HMC method can move a distance $\mathcal{O}(1)$ in the parameter space. This means that HMC degenerates at rate σ^{-1} as $\sigma \rightarrow 0$.

Riemannian-manifold Hamiltonian Monte Carlo (RM-HMC) [GC11] and related position-dependent MALA [RS02, XSL⁺14]) and RWM [Liv15] methods use a position-dependent metric to locally rescale the

target distribution or, equivalently, locally rescale the size of the proposed moves in different directions. For an appropriate choice of metric which differentially rescales proposed moves along the tangential and orthogonal direction of the limiting manifold structure, these approaches may seem to offer a potential solution to degeneration in performance of the standard RWM, MALA and HMC algorithms as $\sigma \rightarrow 0$. In practice however these approaches still require the use of a vanishing step size as $\sigma \rightarrow 0$ in order to maintain a non-zero acceptance rate, as shown in the bottom-centre panel in Figure 2. The metric used was the expected Fisher information matrix plus prior covariance, as recommended by [GC11], which has the desired behaviour of rescaling the steps to make small moves normal to and large moves tangential to the limiting manifold. Despite this the RM-HMC chains show the same pattern as HMC with a fixed metric of requiring $\epsilon \propto \sigma$ to maintain a non-vanishing acceptance rate as $\sigma \rightarrow 0$.

At a high-level, this phenomena can be attributed to the fact that, although the corresponding continuous time dynamics underlying RM-HMC and related approaches ‘follow’ the curvature of the limiting manifold, for a finite discretisation step size the simulated trajectories only approximately replicate this idealized dynamic. In particular, as $\sigma \rightarrow 0$, smaller steps are needed for the dynamics to remain adequately close to the limiting manifold for the acceptance probability to remain non-zero and to ensure the iterative solvers used in the (implicit) generalised leapfrog integrator required by the RM-HMC algorithm do not diverge.

In contrast to the aforementioned standard HMC and RM-HMC approaches, the *constrained Hamiltonian Monte Carlo* (c-HMC) method proposed in this paper is able to maintain a constant acceptance rate when using a fixed integrator step size ϵ as $\sigma \rightarrow 0$. This is shown for c-HMC chains running in the toy example in the bottom-right panel of Figure 2. When combined with the coherent (non-diffusive) exploration of the state space afforded by the Hamiltonian dynamics based proposals, this means the methodology we propose allows efficient MCMC based estimates in the vanishing noise regime.

3 Lifting the posterior distribution onto a manifold

In this section, we describe our approach for constructing a MCMC method which allows us to efficiently approximate expectations with respect to the posterior distribution $\pi^\sigma(d\theta)$ in the $\sigma \rightarrow 0$ asymptotic. Our approach relies on considering an extended state-space $\mathcal{X} \equiv \Theta \times \mathcal{Y} \equiv \mathbb{R}^{d_{\mathcal{X}}}$, with dimension $d_{\mathcal{X}} = d_{\Theta} + d_{\mathcal{Y}}$, of pairs $q = (\theta, \eta) \in \mathcal{X}$ and an extended auxiliary distribution $\bar{\pi}^\sigma(dq) = \bar{\pi}^\sigma(d\theta, d\eta)$ that has the posterior distribution $\pi^\sigma(d\theta)$ as θ -marginal, and constructing a Markov chain which leaves this extended distribution invariant. For this approach to be computationally viable, designing a rapidly mixing Markov chain that leaves the extended distribution $\bar{\pi}^\sigma(d\theta, d\eta)$ invariant should be easier than constructing a rapidly mixing ergodic Markov chain with respect to the original distribution $\pi^\sigma(d\theta)$.

Before describing the construction of the extended distribution $\bar{\pi}^\sigma(dq)$ our method is based upon, we recall a few standard results on conditioning of random variables. Consider a random variable Q with density $\pi : \mathcal{X} \rightarrow \mathbb{R}_{\geq 0}$ with respect to the Lebesgue measure on \mathcal{X} , as well as a continuously differentiable mapping $C : \mathcal{X} \rightarrow \mathcal{Y}$ whose Jacobian matrix $\mathbf{DC}(q)$ has full-rank for μ -almost every $q \in \mathcal{X}$. A consequence of the co-area formula [RSL10, DHS13, GS17] gives that, for any test function $\varphi : \mathcal{X} \rightarrow \mathbb{R}$, we have that

$$\mathbb{E}[\varphi(Q) | C(Q) = 0] = \frac{1}{\mathcal{Z}} \int_{\mathcal{M}} \varphi(q) J(q)^{-1} \pi(q) \mathcal{H}(dq) \quad (4)$$

where $\mathcal{Z} = \int_{\mathcal{M}} J(q)^{-1} \pi(q) \mathcal{H}(dq)$ is a normalization constant and $\mathcal{H}(dq)$ is the $d_{\mathcal{M}}$ -dimensional Hausdorff (uniform) measure on the manifold

$$\mathcal{M} = C^{-1}(0) = \{q \in \mathcal{X} : C(q) = 0\}. \quad (5)$$

This manifold has dimension $d_{\mathcal{M}} \equiv d_{\mathcal{X}} - d_{\mathcal{Y}} = d_{\Theta}$. The quantity $J(q)$ is given by the square-root of the determinant of the Gramian matrix $\mathbf{G}(q) \equiv \mathbf{DC}(q) \mathbf{DC}(q)^{\top} \in \mathbb{R}^{d_{\mathcal{Y}} \times d_{\mathcal{Y}}}$ of the mapping C ,

$$J(q) \equiv \det \left(\mathbf{DC}(q) \mathbf{DC}(q)^{\top} \right)^{1/2}.$$

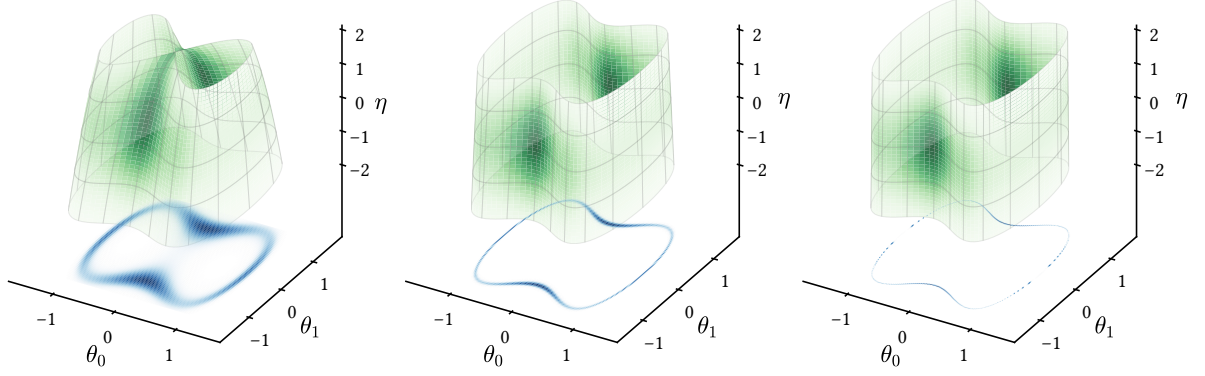


Figure 3: Manifold \mathcal{M} and density $\bar{\pi}^\sigma$ (green) in the extended space \mathcal{X} for $\sigma \in \{0.5, 0.1, 0.02\}$ (left-to-right). Only subset of \mathcal{M} with $|\eta| \leq 2$ is shown. The density π^σ on Θ (blue) is shown for comparison.

The statistical model (1) where $y = F(\theta) + \sigma \eta$ corresponds to the case where the constraint mapping $C : \mathcal{X} \rightarrow \mathcal{Y}$ reads

$$C(q) = C(\theta, \eta) = F(\theta) + \sigma \eta - y.$$

It then follows that the Gramian matrix $\mathbf{G}(q)$ of the constraint mapping C reads

$$\mathbf{G}(q) = \mathbf{G}(\theta, \eta) = \mathbf{D}F(\theta) \mathbf{D}F(\theta)^\top + \sigma^2 \mathbf{I}_{d_y}, \quad (6)$$

with for any choice of $\sigma > 0$ the Gramian matrix $\mathbf{G}(q)$ being positive definite, and hence invertible. Since a-priori $\eta \sim \mathcal{N}(0, \mathbf{I}_{d_y})$ and the prior density on the unknown parameter θ is proportional to $\exp[-\Phi_0(\theta)]$, we have that $-\log \pi(\theta, \eta) = \Phi_0(\theta) + (1/2) \|\eta\|^2$. Consequently, Equation (4) implies that the posterior distribution on the pair $q = (\theta, \eta)$ has a density $\bar{\pi}^\sigma(\theta, \eta)$ with respect to the Hausdorff measure $\mathcal{H}(dq)$ on the manifold $\mathcal{M} \equiv C^{-1}(0)$ given by

$$-\log \bar{\pi}^\sigma(\theta, \eta) = \Phi_0(\theta) + \frac{1}{2} \|\eta\|^2 + \frac{1}{2} \log \det \mathbf{G}(\theta, \eta) + \text{constant}. \quad (7)$$

Note that the manifold $\mathcal{M} \subset \mathcal{X}$ depends on the intensity $\sigma > 0$ of the additive Gaussian noise,

$$\mathcal{M} = \{(\theta, \eta) \in \mathcal{X} : y = F(\theta) + \sigma \eta\}. \quad (8)$$

In the running example (3), the original parameter space Θ is two-dimensional and, as $\sigma \rightarrow 0$, the posterior distribution concentrates in a neighbourhood of the one-dimensional manifold \mathcal{S} . Figure 3 shows the two-dimensional manifold \mathcal{M} embedded in the three-dimensional extended space \mathcal{X} and the extended posterior density $\bar{\pi}^\sigma$ on the manifold for $\sigma \in \{0.5, 0.1, 0.02\}$. It can be seen that though the geometry of the manifold does change as $\sigma \rightarrow 0$, unlike the posterior distribution with density π^σ in the original space Θ , the extended posterior distribution with density $\bar{\pi}^\sigma$ on the manifold does not concentrate and remains diffuse. Furthermore, at an heuristic level at least, note that as $\sigma \rightarrow 0$ the manifold \mathcal{M} ‘tends’ towards the product manifold $\{(\theta, \eta) \in \Theta \times \mathcal{Y} : y = F(\theta)\} \equiv \mathcal{S} \times \mathcal{Y}$. This phenomenon partly motivates why our proposed methodology does not degenerate as $\sigma \rightarrow 0$.

In summary, the extended distribution $\bar{\pi}^\sigma(\theta, \eta)$ can be described as the prior density $\pi_0(\theta) \otimes \pi_0(\eta)$ constrained on the manifold \mathcal{M} dictated by the forward operator F , with an additional multiplicative term $J(q)$ to account for the non-linear transformation of space $\Theta \rightarrow \mathcal{M}$. Our method consists in lifting the posterior distribution π^σ that is concentrated in the neighbourhood of a set $\mathcal{S} \subset \Theta$ onto a manifold \mathcal{M} in a higher dimensional space $\mathcal{X} \equiv \Theta \times \mathcal{Y}$, with the problem transformed into that of sampling from the lifted distribution $\bar{\pi}^\sigma$ supported on \mathcal{M} . Importantly the lifted posterior distribution remains diffuse in the vanishing noise limit $\sigma \rightarrow 0$. We propose to use a constrained HMC algorithm to efficiently sample from the manifold-supported extended distribution $\bar{\pi}^\sigma$ using first- and second-order derivative information. As will be numerically demonstrated in Section 5, the resulting sampler does not degenerate as $\sigma \rightarrow 0$.

that the momentum p (under an assumption of an identity metric equivalent to the velocity) is in the tangent space $\mathcal{T}_{\mathcal{M}}(q)$ at $q \in \mathcal{M}$ at all time points.

Constrained HMC operates on the same principles as standard HMC, however additional projection steps are necessary in the integrator used to ensure that the position q remains on the manifold \mathcal{M} and that the momentum p remain in the tangent space $\mathcal{T}_{\mathcal{M}}(q)$ at all time steps. The resulting *constrained leapfrog integrator* [LM16], summarised in Algorithm 2 and visualised in Figure 4, is a variant of the *RATTLE integrator* [And83] with an additional intermediate momentum projection, and, subject to appropriate definitions of the projection functions, is volume-preserving [LS94, Rei96]. As will be described in Section 4.3, additional *reversibility checks* also ensure the reversibility of the method.

Algorithm 2 Constrained leapfrog integrator

Inputs: $\{p_0, q_0, \epsilon\}$ see Algorithm 1, τ tolerance and M maximum iterations for position projection.

Outputs: $\{p_1, q_1\}$ see Algorithm 1, FAILED flag for failed position projection.

function CONSTRAINEDSTEP($p_0, q_0, \epsilon, \tau, M$)

$\tilde{p}_{1/2} \leftarrow p_0 - \frac{\epsilon}{2} \nabla U(q_0)$ $\tilde{p}_{1/2} \leftarrow \text{PROJECTMOMENTUM}(\tilde{p}_{1/2}, q_0)$ $\tilde{q}_1 \leftarrow q_0 + \epsilon \tilde{p}_{1/2}$ $q_1, \text{FAILED} \leftarrow \text{PROJECTPOSITION}(\tilde{q}_1, q_0, \tau, M)$ $p_{1/2} = \frac{1}{\epsilon}(q_1 - q_0)$ $\tilde{p}_1 \leftarrow p_{1/2} - \frac{\epsilon}{2} \nabla U(q_1)$ $p_1 \leftarrow \text{PROJECTMOMENTUM}(\tilde{p}_1, q_1)$ return p_1, q_1, FAILED	\triangleright Unconstrained momentum half-step update \triangleright Project $\tilde{p}_{1/2}$ onto $\mathcal{T}_{\mathcal{M}}(q_0)$ (see §4.1) \triangleright Unconstrained position full-step update \triangleright Project \tilde{q}_1 onto \mathcal{M} (see §4.2) \triangleright Compute $p_{1/2}$ such that $q_1 = q_0 + \epsilon p_{1/2}$ \triangleright Unconstrained momentum half-step update \triangleright Project \tilde{p}_1 onto $\mathcal{T}_{\mathcal{M}}(q_1)$
--	--

4.1 Momentum projection

The constrained integrator in Algorithm 2, uses a function `PROJECTMOMENTUM`, which orthogonally projects a momentum $\tilde{p} \in \mathbb{R}^{d_x}$ onto $\mathcal{T}_{\mathcal{M}}(q)$ at a position $q \in \mathcal{M}$. The projected momentum p can be expressed as $p = \tilde{p} - \mathbf{DC}(q)^\top \mu$ for a vector $\mu \in \mathbb{R}^{d_y}$ as the rows of $\mathbf{DC}(q)$ span $\mathcal{N}_{\mathcal{M}}(q)$. Solving the equation $\mathbf{DC}(q) (\tilde{p} - \mathbf{DC}(q)^\top \mu) = 0$ for μ gives that

$$p = \text{PROJECTMOMENTUM}(\tilde{p}, q) = \left(\mathbf{I}_{d_x} - \mathbf{DC}(q)^\top \mathbf{G}(q)^{-1} \mathbf{DC}(q) \right) \tilde{p}. \quad (9)$$

Since the Gramian matrix $\mathbf{G}(q)$ is positive definite, the projection operator (9) is well-defined.

4.2 Position projection

In order to implement the constrained integrator, we need to be able to project along $\mathcal{N}_{\mathcal{M}}(q)$ an arbitrary position $\tilde{q} \in \mathcal{X}$ onto the manifold \mathcal{M} . In other words, one needs to solve the non-linear equation

$$\chi(\mu) \equiv C(\tilde{q} - \mathbf{DC}(q)^\top \mu) = 0. \quad (10)$$

A range of numerical methods can be potentially used for solving Equation (10). We advocate using a quasi-Newton approach called the *symmetric Newton method* [BKLS95], as also considered in [GS17]. Implementing a standard Newton approach reduces to iterating updates

$$\mu_{m+1} = \mu_m + \left[\mathbf{DC}(q_m) \mathbf{DC}(q)^\top \right]^{-1} \chi(\mu_m), \quad (11)$$

with $q_m = \tilde{q} - \mathbf{DC}(q)^\top \mu_m$. This requires a matrix solve operation plus an evaluation of the constraint Jacobian \mathbf{DC} at each Newton iteration. The symmetric Newton method instead iterates

$$\mu_{m+1} = \mu_m + \mathbf{G}(q)^{-1} \chi(\mu_m), \quad (12)$$

with a fixed (with respect to m) preconditioning matrix $\mathbf{G}(q)^{-1}$. This is motivated by the observation that the matrix $\mathbf{D}C(q_m)\mathbf{D}C(q)^\top$ usually stays largely constant over the Newton iterations [BKLS95].

Recall that the matrix $\mathbf{G}(q)$ is positive definite, and therefore we can perform a single Cholesky decomposition of it, *once per constrained integrator step*. Each iteration in 12 then only requires an evaluation of the constraint function to compute $v = \chi(\mu_m)$ and a quadratic cost solve to compute $\mathbf{G}(q)^{-1}v$. Further we can also use the Gramian matrix Cholesky factor to efficiently calculate the $\log \det \mathbf{G}(q)$ term (and its derivative) in the potential energy $U(q)$.

In practice, we stop the iteration (12) as soon as the norm $\|\chi(\mu_m)\|_\infty = \|C(q_m)\|_\infty$ falls below a tolerance threshold τ , or a maximum number M of iterations is reached. We suggest setting τ such that the projection error is comparable to the numerical error already incurred from using floating-point arithmetic. Furthermore, as mentioned in [ZHCG18], we also recommend setting the maximum number of iterations M relatively small. In doing so, we avoid wasting computational effort on proposals whose position projections take too long to converge by quickly rejecting them in search for better ones. In our work, we set $\tau = 10^{-8}$ and $M = 50$, and the average number of iterations to convergence in practice was around 5 to 10 in our experiments. In the case when the quasi-Newton iterations do not converge, which does happen for a non-negligible fraction of the proposals, the proposal is rejected. As explain in the next section, the possible non-convergence of the quasi-Newton iterates, as well as the possible existence of multiple solutions to the non-linear Equation (10), require us to perform some additional checks to avoid compromising the correctness of the overall method.

4.3 Reversibility check

The correctness of the standard HMC method is ensured by the reversibility and volume preservation of the leapfrog integrator. Although the constrained integrator is also volume-preserving (as a consequence of being symplectic [LS94, Rei96]), the reversibility property needs to be checked more carefully. This is because the non-linear equation (10) that needs to be solved to implement the PROJECTPOSITION function may not have a single unique solution, and the numerical method used to find such the solution may not converge within a prescribed number of iterations¹.

To enforce reversibility we follow the scheme proposed by [ZHCG18] (for a constrained RWM algorithm) by manually checking if each constrained step constitutes a reversible map. For each forward step $(q, p) \rightarrow (q', p')$, we run the step in reverse (by negating the time step) $(q', p') \rightarrow (q^*, p^*)$. We proceed with the next step only if the current step is reversible, i.e., $(q, p) = (q^*, p^*)$ to within a numerical tolerance ρ , and neither of the iterative solves in the position projections in the forward nor reverse steps failed to converge (indicated by the FAILED flag returned by the PROJECTPOSITION function in Algorithm 2 being TRUE); otherwise the trajectory terminates early and we reject. By construction this reversibility check guarantees the overall simulated trajectory defines a reversible map.

In terms of the additional cost of this reversibility check, the main expensive quantities necessary for the reverse step — the constraint Jacobian and Grammian matrix decomposition — will also be required in the subsequent forward step if the reversibility check is successful. Hence, by caching these quantities in memory, the marginal costs of computing the reverse step amount to at most M evaluations of the constraint function (and so F) in the reverse step position projection.

4.4 Practical implementation

We now discuss strategies for efficiently evaluating the quantities involving the Gramian matrix

$$\mathbf{G}(q) = \mathbf{G}(\theta, \eta) = \mathbf{D}F(\theta)\mathbf{D}F(\theta)^\top + \sigma^2\mathbf{I}_{d_y} \in \mathbb{R}^{d_y \times d_y}.$$

¹For sufficiently small step sizes, the constrained integrator is in fact reversible. For a detailed numerical analysis of the closely related RATTLE integrator [And83] when combined with a Newton iteration to solve the position projection, see [LRS19]. Nevertheless, there is currently no practical way to identify such a step size nor would it be useful if the small step size leads to inefficient sampling.

The log-determinant of $\mathbf{G}(q)$ is needed to evaluate the potential energy (7) and we require to solve $\mathbf{G}(q)^{-1}v$ for $v \in \mathbb{R}^{d_y}$ in the momentum and position projections. We now show that the computational cost necessary to evaluate these quantities only scales as $\mathcal{O}(\min(d_\Theta d_y^2, d_y d_\Theta^2))$. As is illustrated in Section 5, standard applications often requires $d_\Theta \ll d_y$ or $d_\Theta \gg d_y$.

Underdetermined systems: $d_\Theta > d_y$.

The case of $d_\Theta > d_y$ is common to inverse problems when observations are few and inference parameters are many. As an example, Section 5.3 describes inverting the stationary heat equation to recover a high-dimensional thermal conductivity field — in this setting d_Θ refers to the dimension of the *finite element method* (FEM) discretization. Since $\mathbf{D}F(\theta) \in \mathbb{R}^{d_y \times d_\Theta}$, forming the Gramian matrix $\mathbf{G}(q)$ costs $\mathcal{O}(d_\Theta d_y^2)$ while computing its Cholesky decomposition scales as $\mathcal{O}(d_y^3)$, from which both $\det \mathbf{G}(q)$ and $\mathbf{G}(q)^{-1}v$ can be computed at $\mathcal{O}(d_y)$ cost. Overall therefore the computational cost scales as $\mathcal{O}(d_\Theta d_y^2)$.

Overdetermined systems: $d_y > d_\Theta$.

When the dimensionality of the observations exceeds the dimensionality of the latent space, the system is overdetermined, as exemplified in Section 5.2. In order to avoid computations that scale cubically in d_y when evaluating the determinant of $\mathbf{G}(q)$, one can use the Weinstein–Aronszajn identity,

$$\det \mathbf{G}(q) = \sigma^{2d_y} \det \left[\sigma^{-2} \mathbf{D}F(\theta) \mathbf{D}F(\theta)^\top + \mathbf{I}_{d_y} \right] = \sigma^{2d_y} \det \left[\sigma^{-2} \mathbf{D}F(\theta)^\top \mathbf{D}F(\theta) + \mathbf{I}_{d_\Theta} \right],$$

which can be computed in $\mathcal{O}(d_y d_\Theta^2)$ operations. Similarly, using the Woodbury identity we have that

$$\mathbf{G}(q)^{-1} = \sigma^2 \left\{ \mathbf{I}_{d_y} - \mathbf{D}F(\theta) \left[\sigma^2 \mathbf{I}_{d_\Theta} + \mathbf{D}F(\theta)^\top \mathbf{D}F(\theta) \right]^{-1} \mathbf{D}F(\theta)^\top \right\} \quad (13)$$

which can be used to solve $\mathbf{G}(q)^{-1}v$ at $\mathcal{O}(d_y d_\Theta^2)$ computational cost.

4.5 Complete algorithm

Recall that the target distribution $\bar{\pi}^\sigma(dq)$ is supported on the manifold \mathcal{M} and has a density given by

$$\frac{d\bar{\pi}^\sigma}{d\mathcal{H}}(q) = \frac{d\bar{\pi}^\sigma}{d\mathcal{H}}(\theta, \eta) \propto \exp \left\{ -\Phi_0(\theta) - \frac{1}{2} \|\eta\|^2 - \frac{1}{2} \log \det \mathbf{G}(\theta, \eta) \right\}.$$

Consequently, for c-HMC with an identity mass matrix, the Hamiltonian reads

$$H(q, p) = H((\theta, \eta), p) = \Phi_0(\theta) + \frac{1}{2} \|\eta\|^2 + \frac{1}{2} \log \det \mathbf{G}(\theta, \eta) + \frac{1}{2} \|p\|^2.$$

For initializing the c-HMC algorithm, one can choose an arbitrary initial $\theta_0 \in \Theta$ (e.g. by sampling from the prior) and map to the corresponding unique extended state $q_0 = (\theta_0, [y - F(\theta_0)]/\sigma) \in \mathcal{M}$. Algorithm 3 provides a complete description of a single chain transition of the c-HMC method.

Interestingly, the constrained continuous-time Hamiltonian dynamic on \mathcal{M} underlying the method proposed in this paper admits an equivalent formulation as a Hamiltonian dynamic on the original state space Θ equipped with a particular Riemannian metric (see Appendix A). Importantly however, the constrained integrator used in our extended state space formulation is both significantly cheaper to run than the generalized leapfrog integrator typically used in RM-HMC and overcomes the issues underlying the collapse of the RM-HMC acceptance rate in the $\sigma \rightarrow 0$ limit observed in Section 2.

5 Numerical experiments

In this section, we evaluate the performance of our proposed method on several inference problems. Standard HMC with an identity metric is chosen as the benchmark method for unconstrained MCMC sampling, other than for the first (toy) example for which we also compare to RM-HMC. We use a

Algorithm 3 c-HMC transition

Inputs: q current position, N number of integrator steps per transition, ρ reversibility check tolerance, $\{\epsilon, \tau, M\}$ see Algorithm 2.

Outputs: q' updated position such that $q \sim \bar{\pi}^\sigma(\cdot) \implies q' \sim \bar{\pi}^\sigma(\cdot)$.

```
function CONSTRAINEDHMC( $q, \epsilon, \tau, \rho, N, M$ )  
   $q_0 \leftarrow q$   
   $\tilde{p}_0 \leftarrow \mathcal{N}(0, \mathbf{I}_{d_X})$  ▷ Sample momentum from standard Gaussian  
   $p_0 \leftarrow \text{PROJECTMOMENTUM}(\tilde{p}_0, q_0)$   
  for  $n \in \{1, \dots, N\}$  do  
     $q_n, p_n, \text{FWFAILED} \leftarrow \text{CONSTRAINEDSTEP}(q_{n-1}, p_{n-1}, \epsilon, \tau, M)$  ▷ Forward step  
     $q_*, p_*, \text{RVFAILED} \leftarrow \text{CONSTRAINEDSTEP}(q_n, p_n, -\epsilon, \tau, M)$  ▷ Reverse step  
    if  $\text{FWFAILED}$  or  $\text{RVFAILED}$  or  $\|q_* - q_{n-1}\|_\infty \geq \rho$  then ▷ Reversibility check  
      return  $q$  ▷ Reject proposal if non-reversible  
  if  $\text{uniform}(0, 1) < \exp[H(q_0, p_0) - H(q_n, p_n)]$  then ▷ Metropolis acceptance step  
    return  $q_N$  ▷ Accept proposal  
  else  
    return  $q$  ▷ Reject proposal
```

variant of the *No-U-Turn Sampler* (NUTS) algorithm [HG14, Bet17] to automate the tuning of the number of integrator steps in each proposal's trajectory for all three methods. All experiments were performed using the MCMC sampler implementations in the Python package Mici [Gra19], which defines a high-level interface which abstracts away the details of Algorithm 3 and requires only specification of the model functions and optionally, their derivatives. The integrator step size $\epsilon > 0$ for all methods was tuned in short preliminary MCMC runs in order to ensure an acceptance rate in between 0.7 and 0.95. We report the minimum estimated *effective sample size* (ESS) over the d_Θ quantity of interest dimensions, normalised by the total chain run time, as our measure of sampling efficiency. We compute the ESS estimates using the ArviZ [KCHM19] implementation of the *bulk*-ESS statistic proposed in [VGS⁺19].

Our experiments indicate that, as heuristically described in Section 2, standard HMC requires a leapfrog step size $\epsilon \rightarrow 0$ as the posterior distribution concentrates near the limiting manifold \mathcal{S} in order to operate at a reasonable acceptance rate, meaning the sampling efficiency of standard HMC degenerates as $\sigma \rightarrow 0$. In stark contrast, the simulations demonstrate that the sampling efficiency of the c-HMC sampler is robust to the vanishing noise asymptotic. Note that for large values of σ (i.e. when the posterior distribution is not concentrated near low-dimensional structures) standard HMC is typically more sample-efficient than our proposed c-HMC approach due to the higher computational cost of the constrained leapfrog integrator.

5.1 Toy example

We first return to our running toy example considered in Section 2. The top-right panel in Figure 2 shows the sampling efficiencies for standard HMC, RM-HMC and our proposed approach of c-HMC on the extended space. For RM-HMC the same Fisher information based metric is used as described previously. It can be immediately seen that both HMC and RM-HMC degenerate as $\sigma \rightarrow 0$ while the mixing efficiency of the c-HMC is unaffected by the vanishing noise asymptotic. To maintain an acceptance rate of 0.7–0.95, standard HMC required a leapfrog step about 8 times smaller, and RM-HMC around 14 times smaller, than the noise intensity parameter σ . For c-HMC we used a constant leapfrog step size $\epsilon = 8.7 \times 10^{-2}$ for all values of σ .

5.2 FitzHugh–Nagumo ordinary differential equation model

As a second example, we consider parameter inference in a noisily observed non-linear dynamical system. The FitzHugh–Nagumo model [Fit61, NAY62], a simplified description of the dynamics of

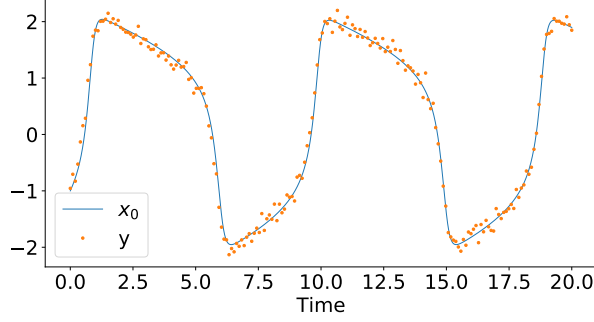


Figure 5: Fitzhugh-Nagumo model: noisy observations from the first coordinate $x_0(t)$.

action potential generation within an neuronal axon, can be described by the following system of ODEs

$$\frac{dx_0}{dt} = \alpha x_0 - \beta x_0^3 + \gamma x_1, \quad \frac{dx_1}{dt} = -\delta x_0 - \epsilon x_1 + \zeta. \quad (14)$$

We use a fourth-order Runge-Kutta method to discretise the system in time, implementing the numerical integration in the Python package JAX [BFH⁺18] to allow use of its automatic differentiation implementation to compute the required derivatives. The ground truth parameter used were $\alpha = 3$, $\beta = 1$, $\gamma = 3$, $\delta = 1/3$, $\epsilon = 1/15$, and $\zeta = 1/15$, and initial state $x(0) = (1, -1)$. As shown in Figure 5, we simulated noisy observations $y_k = x_0(t_k) + \sigma \eta_k$, with $\eta_k \sim \mathcal{N}(0, 1)$, of the first state coordinate $t \mapsto x_0(t)$ at $d_y = 200$ equispaced times $0 = t_1 < \dots < t_{d_y} = 20$. The parametrisation of the Fitzhugh-Nagumo system of ODEs in Equation (14) is non-identifiable. Specifically, the dynamics remains unchanged under the transformation

$$(x_0(0), x_1(0), \alpha, \beta, \gamma, \delta, \epsilon, \zeta) \mapsto (x_0(0), s x_1(0), \alpha, \beta, s^{-1} \gamma, s \delta, \epsilon, s \zeta)$$

for any scaling factor $s > 0$. This means that $x_1(0), \gamma, \delta$ and ζ are only identifiable up to the common scaling factor s . Therefore, the posterior distribution on $x_1(0), \gamma, \delta$ and ζ concentrates around a limiting manifold, as show in the left panel of Figure 6.

We specify the prior distributions as $\log \alpha \sim \mathcal{N}(0, 1)$, $\log \beta \sim \mathcal{N}(0, 1)$, $\log \gamma \sim \mathcal{N}(0, 1)$, $\log \delta \sim \mathcal{N}(-1, 1)$, $\log \epsilon \sim \mathcal{N}(-2, 1)$, $\log \zeta \sim \mathcal{N}(-2, 1)$, $x_0(0) \sim \mathcal{N}(0, 1)$, and $x_1(0) \sim \mathcal{N}(0, 1)$, using a logarithmic parametrisation for $(\beta, \gamma, \delta, \epsilon, \zeta)$ to enforce non-negativity constraints. To maintain an acceptance rate of about 0.8, standard HMC required a leapfrog step about 200 times smaller than the noise intensity parameter σ . For c-HMC, the leapfrog step was set to $\epsilon = 0.5$ for all values of σ . Figure 6 shows that, as $\sigma \rightarrow 0$, the sampling efficiency of standard HMC degenerates. On the other hand, our method is robust to $\sigma \rightarrow 0$.

5.3 Non-linear Poisson partial differential equation model

Consider a two-dimensional domain $\Omega \subset \mathbb{R}^2$ and the problem of inferring the log-conductivity field $\Phi : \Omega \rightarrow \mathbb{R}$ from a discrete set of noisy observations of the temperature field $u : \Omega \rightarrow \mathbb{R}$ and a known source term $\mathcal{F} : \Omega \rightarrow \mathbb{R}$. These quantities satisfy the following Poisson PDE on the domain Ω ,

$$-\nabla \cdot (e^\Phi \nabla u) = \mathcal{F}, \quad (15)$$

with vanishing Dirichlet boundary conditions $u|_{\partial\Omega} = 0$. Noisy observations of the temperature field $y_k = u(x_k) + \sigma \eta$, with $\eta \sim \mathcal{N}(0, 1)$, are available at $d_y = 5$ distinct locations $x_k \in \Omega$, as depicted in Fig 7. The library FEniCS [ABH⁺15] is used to numerically solved the PDE (15) with a first order FEM on a standard triangular discretization of Ω with dimension $d_\Theta = 207$. This means that the discretised log-conductivity field can be expressed as $\Phi(x) = \sum_{k=1}^{d_\Theta} \alpha_k e_k(x)$ for linear basis functions $e_k : \Omega \rightarrow \mathbb{R}$ and coefficients $\alpha = (\alpha_1, \dots, \alpha_{d_\Theta}) \in \Theta \equiv \mathbb{R}^{d_\Theta}$. We use a standard Gaussian field with a Matérn

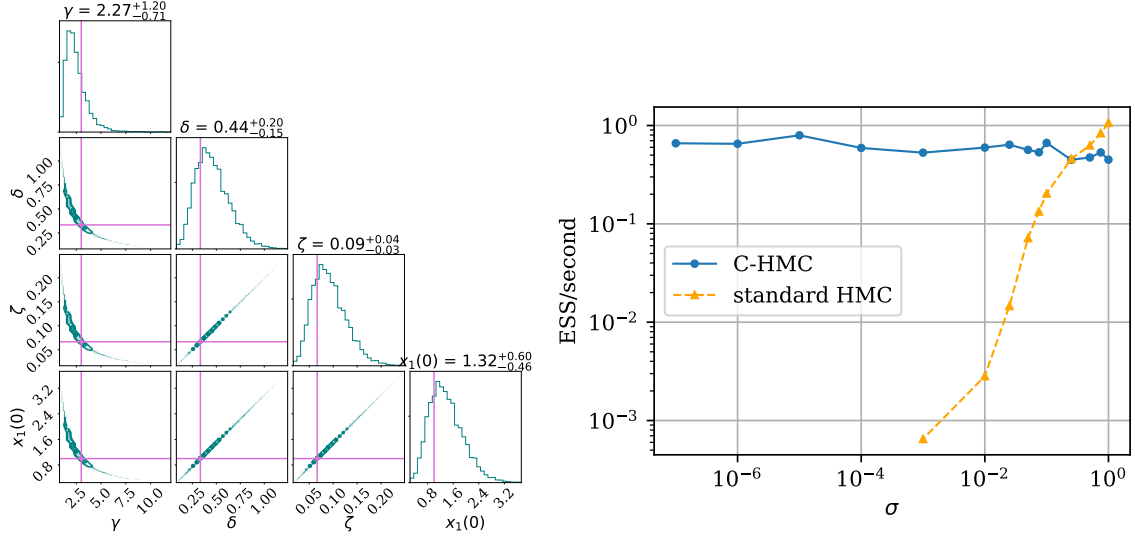


Figure 6: ODE parameters inference. Left: C-HMC posterior samples with ground truth in magenta. Right: sampling efficiency as $\sigma \rightarrow 0$. For standard HMC the time-normalized ESS estimates in the vanishing noise regime that are not reliable due to insufficiently converged chains are not shown.

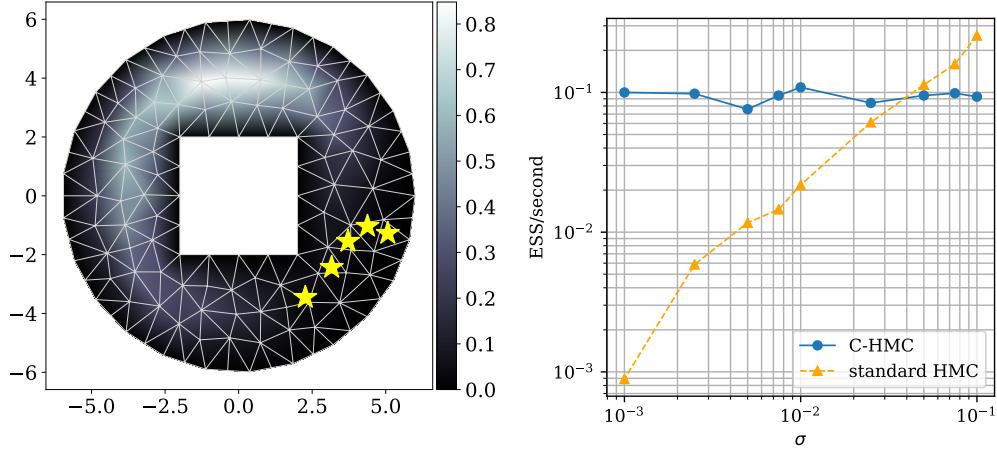


Figure 7: Log-conductivity field inference. (left): posterior marginal standard deviation of the solution fields $u : \Omega \rightarrow \mathbb{R}$ inferred from C-HMC samples. The standard deviations are particularly low near observation points (yellow stars), corresponding to regions of low uncertainty in our inference. (right): sampling efficiency as $\sigma \rightarrow 0$.

covariance [LRL11] as prior distribution on Φ . This can be realized as a FEM discretization of the Poisson equation $(\kappa^2 - \Delta)\Phi = \mathcal{W}$, with scaling parameter $\kappa = 0.1$, for a spatial Gaussian white noise $\mathcal{W} : \Omega \rightarrow \mathbb{R}$ with unit variance. This induces a centred Gaussian prior on the coefficients $\alpha \in \Theta$ with covariance matrix $\Gamma \in \mathbb{R}^{d_\Theta \times d_\Theta}$. For implementing the method, we choose a centred parametrization $\alpha = \Gamma^{1/2} \theta$, for unknown parameter vector $\theta \in \Theta$. Our objective is to explore the Bayesian posterior on the vector of coefficients θ given the set of observations (y_1, \dots, y_{d_Y}) . Note that each evaluation of the posterior density involves solving the Poisson Equation (15). Figure 7 shows that the standard HMC method degenerates as $\sigma \rightarrow 0$, contrarily to our proposed method that is robust to the vanishing noise regime.

6 Conclusion

While a large literature has been devoted to designing MCMC samplers with good mixing properties when used in high-dimensional settings, comparatively little attention has been devoted to the problem of exploring distributions concentrating near low-dimensional manifolds or exhibiting multi-scale structures [BRT18, SSW19]. To the best of our knowledge, the sampling efficiency of all currently existing general-purpose MCMC samplers degenerates in the vanishing noise $\sigma \rightarrow 0$ asymptotic studied in this text. By reformulating the original problem into the task of exploring a distribution supported on a manifold embedded in a higher dimensional space, our proposed methodology is able to maintain high sampling efficiency in the $\sigma \rightarrow 0$ regime. Our work opens up a number of avenues for future work in this area. While we concentrated in this work on additive, isotropic Gaussian observation noise, there are natural possible extensions to more general observation processes. Furthermore, an important open question is whether it is possible to define variants of the proposed approach that improve scalability in the regime where both observation and latent dimensions, d_Θ and d_Y , are high, with the current scheme having a $\mathcal{O}(\min(d_\Theta d_Y^2, d_Y d_\Theta^2))$ computational complexity.

Acknowledgments

The authors acknowledge support from a National University of Singapore (NUS) Young Investigator Award Grant (R-155-000-180-133) and a Singapore Ministry of Education Academic Research Funds Tier 2 (MOE2016-T2-2-135).

A Equivalent Hamiltonian dynamic in Θ space

In this paper we construct an MCMC method targetting a distribution defined on a space $\Theta \subseteq \mathbb{R}^{d_\Theta}$ by simulating a Hamiltonian dynamic defined on a d_Θ -dimensional manifold \mathcal{M} embedded in an extended state space $\mathcal{X} \equiv \Theta \times \mathcal{Y}$. We implicitly define \mathcal{M} via a constraint equation

$$\mathcal{M} = \{(\theta, \eta) \in \mathcal{X} : F(\theta) + \sigma\eta = y\},$$

as this leads naturally to a construction for defining flows on \mathcal{M} via the simulation of the dynamics of a constrained Hamiltonian system, and so our suggested c-HMC approach to inference.

In our specific setting \mathcal{M} can also however be defined as the *graph* of a function $\gamma(\theta) = \frac{y - F(\theta)}{\sigma}$, i.e. $\mathcal{M} = \{(\theta, \gamma(\theta)) : \theta \in \Theta\}$, or equivalently defining $\psi(\theta) = (\theta, \gamma(\theta))$ then $\mathcal{M} = \psi(\Theta)$. If γ is smooth, which will be the case if F is smooth (and $\sigma \neq 0$), then ψ is a diffeomorphism and \mathcal{M} is diffeomorphic to Θ . This has practical consequences in for example ensuring that if Θ is simply-connected and F is smooth then \mathcal{M} will also be simply-connected, thus avoiding the ergodicity issues that would arise in applying the c-HMC method if \mathcal{M} consisted of a set of disconnected components.

That \mathcal{M} is diffeomorphic to the original latent space Θ also means that there is an equivalent Hamiltonian dynamic on Θ to the constrained Hamiltonian dynamic we use to simulate flows on \mathcal{M} . If we denote the momentum variable associated with the dynamics on Θ as $\nu \in \mathbb{R}^{d_\Theta}$, then under

the *canonical transformation* $(q, p) = \Psi(\nu, \theta) = (\psi(\theta), \mathbf{D}\psi(\theta) (\mathbf{D}\psi(\theta)^\top \mathbf{D}\psi(\theta))^{-1} \nu)$, the form of Hamilton's equations is preserved [LR04, §7.6.2]; that is solutions $(\theta(t), \nu(t))_{t \in \mathcal{T}}$ and $(q(t), p(t))_{t \in \mathcal{T}}$ to respectively the ODE systems $(\dot{\theta}, \dot{\nu}) = (\nabla_\nu, -\nabla_\theta) \tilde{H}(\theta, \nu)$ and $(\dot{q}, \dot{p}) = (\nabla_p, -\nabla_q) H(q, p)$ where $\tilde{H}(\theta, \nu) \equiv H \circ \Psi(\nu, \theta)$, satisfy $(q(t), p(t)) = \Psi(\theta(t), \nu(t))$ for all $t \in \mathcal{T}$.

Recalling the previous definition for $H(q, p)$ in our setting

$$H(q, p) = H((\theta, \eta), p) = \Phi_0(\theta) + \frac{1}{2} \|\eta\|^2 + \frac{1}{2} \log \det \mathbf{G}(\theta, \eta) + \frac{1}{2} \|p\|^2,$$

it is simple to show that the equivalent Hamiltonian $\tilde{H}(\theta, \nu)$ can be expressed

$$\tilde{H}(\theta, \nu) = \Phi_0(\theta) + \frac{1}{2\sigma^2} \|y - F(\theta)\|^2 + d_Y \log \sigma + \frac{1}{2} \log \det \mathbf{M}(\theta) + \frac{1}{2} \nu^\top \mathbf{M}(\theta)^{-1} \nu,$$

where $\mathbf{M}(\theta) = \mathbf{D}\psi(\theta)^\top \mathbf{D}\psi(\theta) = \mathbf{I}_{d_\Theta} + \frac{1}{\sigma^2} \mathbf{D}F(\theta)^\top \mathbf{D}F(\theta)$ and we have used that

$$\log \det \mathbf{G}(\theta, \eta) = \log \det \mathbf{M}(\theta) + 2d_Y \log \sigma.$$

This equivalent Hamiltonian $\tilde{H}(\theta, \nu)$ and corresponding dynamic on the original Θ space, is exactly that simulated to generate proposals by RM-HMC when targetting the posterior distribution π^σ on the original space Θ with a metric $\mathbf{M}(\theta)$. For the assumed additive Gaussian isotropic observation noise model, the metric $\mathbf{M}(\theta)$ is equal to the expected Fisher information $\frac{1}{\sigma^2} \mathbf{D}F(\theta)^\top \mathbf{D}F(\theta)$ plus the prior covariance \mathbf{I}_{d_Θ} , i.e. corresponding to the form of metric suggested by [GC11] and used in our experimental comparison in Section 2.

From this equivalence of the continuous-time dynamics, the observed performance differences between our proposed C-HMC approach and RM-HMC (with a specific choice of metric) can be seen to be directly a consequence of the improved performance of the constrained leapfrog integrator used for C-HMC compared to the generalised leapfrog integrator used by RM-HMC. Although both involve implicit steps, as described in the main paper, a symmetric Newton approach can be used to efficiently solve the non-linear system of equations required to implement the position projection in the constrained leapfrog integrator, with each iteration only requiring evaluation of the forward operator F .

In contrast in each generalised leapfrog step, two separate systems of non-linear equations must be solved, with existing implementations generally using a simple direct fixed point iteration [GC11]. Empirically we observe that these simple fixed point iterations have a much higher tendency to diverge or converge slowly compared to the symmetric Newton iteration used for the constrained integrator, and further as each iteration requires re-evaluating the inverse of the metric or a derivative of the inverse metric, the iterations are also typically significantly more expensive to compute. We also stress that the possibility of the fixed point solvers failing to converge, or converging to a different solution in a time-reversed step, mean a similar reversibility check as we use in our C-HMC algorithm, (as originally proposed in a constrained RWM setting by [ZHCG18]), is required to ensure the correctness of the RM-HMC transitions; the RM-HMC implementation we used in experiments [Gra19] includes such checks.

References

- [ABH⁺15] Martin S. Alnæs, Jan Blechta, Johan Hake, August Johansson, Benjamin Kehlet, Anders Logg, Chris Richardson, Johannes Ring, Marie E. Rognes, and Garth N. Wells. The FEniCS project version 1.5. *Archive of Numerical Software*, 3(100), 2015. doi:10.11588/ans.2015.100.20553.
- [And83] Hans C Andersen. RATTLE: A ‘velocity’ version of the SHAKE algorithm for molecular dynamics calculations. *Journal of Computational Physics*, 52(1):24–34, 1983.
- [BCSS14] Sergio Blanes, Fernando Casas, and JM Sanz-Serna. Numerical integrators for the Hybrid Monte Carlo method. *SIAM Journal on Scientific Computing*, 36(4):A1556–A1580, 2014.

- [Bes94] Julian Besag. Comments on ‘Representations of knowledge in complex systems’ by Grenander and Miller. *Journal of the Royal Statistical Society, Series B*, 56:591–592, 1994.
- [Bet17] Michael Betancourt. A conceptual introduction to Hamiltonian Monte Carlo. *arXiv e-prints*, 2017. [arXiv:1701.02434](https://arxiv.org/abs/1701.02434).
- [BFH⁺18] James Bradbury, Roy Frostig, Peter Hawkins, Matthew James Johnson, Chris Leary, Dougal Maclaurin, and Skye Wanderman-Milne. JAX: composable transformations of Python+NumPy programs, 2018. URL: <http://github.com/google/jax>.
- [BKLS95] Eric Barth, Krzysztof Kuczer, Benedict Leimkuhler, and Robert D. Skeel. Algorithms for constrained molecular dynamics. *Journal of Computational Chemistry*, 16(10):1192–1209, 1995. [doi:10.1002/jcc.540161003](https://doi.org/10.1002/jcc.540161003).
- [BPR⁺13] Alexandros Beskos, Natesh Pillai, Gareth Roberts, Jesus-Maria Sanz-Serna, and Andrew Stuart. Optimal tuning of the hybrid Monte Carlo algorithm. *Bernoulli*, 19(5A):1501–1534, 2013.
- [BRT⁺18] Alexandros Beskos, Gareth Roberts, Alexandre Thiery, and Natesh Pillai. Asymptotic analysis of the random walk Metropolis algorithm on ridged densities. *The Annals of Applied Probability*, 28(5):2966–3001, 2018.
- [BSU12] Marcus Brubaker, Mathieu Salzmann, and Raquel Urtasun. A family of MCMC methods on implicitly defined manifolds. In *Proceedings of the Fifteenth International Conference on Artificial Intelligence and Statistics (AISTATS)*, pages 161–172. Proceedings of Machine Learning Research, 2012.
- [DHS13] Persi Diaconis, Susan Holmes, and Mehrdad Shahshahani. *Sampling from a Manifold*, volume Volume 10 of *Collections*, pages 102–125. Institute of Mathematical Statistics, Beachwood, Ohio, USA, 2013. [doi:10.1214/12-IMSCOLL1006](https://doi.org/10.1214/12-IMSCOLL1006).
- [DKPR87] Simon Duane, Anthony D Kennedy, Brian J Pendleton, and Duncan Roweth. Hybrid Monte Carlo. *Physics letters B*, 195(2):216–222, 1987.
- [Fit61] Richard FitzHugh. Impulses and physiological states in theoretical models of nerve membrane. *Biophysical Journal*, 1(6):445–466, 1961.
- [GC11] Mark Girolami and Ben Calderhead. Riemann manifold Langevin and Hamiltonian Monte Carlo methods. *Journal of the Royal Statistical Society: Series B (Statistical Methodology)*, 73(2):123–214, 2011. [doi:10.1111/j.1467-9868.2010.00765.x](https://doi.org/10.1111/j.1467-9868.2010.00765.x).
- [GIKP90] Sourendu Gupta, Anders Irbäck, Frithjof Karsch, and Bengt Petersson. The acceptance probability in the hybrid Monte Carlo method. *Physics Letters, B*, 242(3-4), 1990.
- [Gra19] Matthew M Graham. Mici: manifold MCMC methods in Python, 2019. URL: <https://git.io/mici.py>, [doi:10.5281/zenodo.3600998](https://doi.org/10.5281/zenodo.3600998).
- [GS17] Matthew M Graham and Amos J Storkey. Asymptotically exact inference in differentiable generative models. *Electronic Journal of Statistics*, 11(2):5105–5164, 2017.
- [HG14] Matthew D Hoffman and Andrew Gelman. The No-U-Turn sampler: adaptively setting path lengths in Hamiltonian Monte Carlo. *Journal of Machine Learning Research*, 15(1):1593–1623, 2014.
- [HS05] Carsten Hartmann and Christof Schütte. A constrained hybrid Monte-Carlo algorithm and the problem of calculating the free energy in several variables. *ZAMM-Journal of Applied Mathematics and Mechanics/Zeitschrift für Angewandte Mathematik und Mechanik: Applied Mathematics and Mechanics*, 85(10):700–710, 2005.

- [KCHM19] Ravin Kumar, Colin Carroll, Ari Hartikainen, and Osvaldo A. Martin. ArviZ a unified library for exploratory analysis of Bayesian models in Python. *The Journal of Open Source Software*, 2019. doi:[10.21105/joss.01143](https://doi.org/10.21105/joss.01143).
- [KvdVvZ11] Bartek T Knapik, Aad W van der Vaart, and J Harry van Zanten. Bayesian inverse problems with Gaussian priors. *The Annals of Statistics*, 39(5):2626–2657, 2011.
- [Liv15] Samuel Livingstone. Geometric ergodicity of the random walk Metropolis with position-dependent proposal covariance. *arXiv preprints*, 2015. [arXiv:1507.05780](https://arxiv.org/abs/1507.05780).
- [LM16] Benedict Leimkuhler and Charles Matthews. Efficient molecular dynamics using geodesic integration and solvent–solute splitting. *Proceedings of the Royal Society A: Mathematical, Physical and Engineering Sciences*, 472(2189):20160138, 2016.
- [LR04] Benedict Leimkuhler and Sebastian Reich. *Simulating Hamiltonian dynamics*, volume 14. Cambridge University Press, 2004.
- [LRL11] Finn Lindgren, Håvard Rue, and Johan Lindström. An explicit link between Gaussian fields and Gaussian Markov random fields: the stochastic partial differential equation approach. *Journal of the Royal Statistical Society: Series B (Statistical Methodology)*, 73(4):423–498, 2011.
- [LRS19] Tony Lelièvre, Mathias Rousset, and Gabriel Stoltz. Hybrid Monte Carlo methods for sampling probability measures on submanifolds. *Numerische Mathematik*, 2019. doi:[10.1007/s00211-019-01056-4](https://doi.org/10.1007/s00211-019-01056-4).
- [LS94] Benedict J Leimkuhler and Robert D Skeel. Symplectic numerical integrators in constrained Hamiltonian systems. *Journal of Computational Physics*, 112(1):117–125, 1994.
- [NAY62] Jinichi Nagumo, Suguru Arimoto, and Shuji Yoshizawa. An active pulse transmission line simulating nerve axon. *Proceedings of the IRE*, 50(10):2061–2070, 1962.
- [Nea12] Radford M. Neal. MCMC using Hamiltonian dynamics. *arXiv e-prints*, 2012. [arXiv:1206.1901](https://arxiv.org/abs/1206.1901).
- [PMSG14] Noemi Petra, James Martin, Georg Stadler, and Omar Ghattas. A computational framework for infinite-dimensional Bayesian inverse problems, Part II: Stochastic Newton MCMC with application to ice sheet flow inverse problems. *SIAM Journal on Scientific Computing*, 36(4):A1525–A1555, 2014.
- [Rei96] Sebastian Reich. Symplectic integration of constrained Hamiltonian systems by composition methods. *SIAM Journal on Numerical Analysis*, 33(2):475–491, 1996.
- [RGG97] Gareth O Roberts, Andrew Gelman, and Walter R Gilks. Weak convergence and optimal scaling of random walk Metropolis algorithms. *The Annals of Applied Probability*, 7(1):110–120, 1997.
- [RR01] Gareth O Roberts and Jeffrey S Rosenthal. Optimal scaling for various Metropolis–Hastings algorithms. *Statistical science*, 16(4):351–367, 2001.
- [RS02] Gareth O Roberts and Osnat Stramer. Langevin diffusions and Metropolis–Hastings algorithms. *Methodology and computing in applied probability*, 4(4):337–357, 2002.
- [RSL10] Mathias Rousset, Gabriel Stoltz, and Tony Lelièvre. *Free Energy Computations: A Mathematical Perspective*. Imperial College Press, 2010.

- [SSW19] Claudia Schillings, Björn Sprungk, and Philipp Wacker. On the convergence of the Laplace approximation and noise level robustness of Laplace-based Monte Carlo methods for Bayesian inverse problems. *arXiv preprints*, 2019. [arXiv:1901.03958](https://arxiv.org/abs/1901.03958).
- [Stu10] Andrew M Stuart. Inverse problems: a Bayesian perspective. *Acta numerica*, 19:451–559, 2010.
- [VGS⁺19] Aki Vehtari, Andrew Gelman, Daniel Simpson, Bob Carpenter, and Paul-Christian Bürkner. Rank-normalization, folding, and localization: An improved \hat{R} for assessing convergence of MCMC. *arXiv e-prints*, 2019. [arXiv:1903.08008](https://arxiv.org/abs/1903.08008).
- [XSL⁺14] Tatiana Xifara, Chris Sherlock, Samuel Livingstone, Simon Byrne, and Mark Girolami. Langevin diffusions and the Metropolis-adjusted Langevin algorithm. *Statistics & Probability Letters*, 91:14–19, 2014.
- [ZHCG18] Emilio Zappa, Miranda Holmes-Cerfon, and Jonathan Goodman. Monte Carlo on manifolds: sampling densities and integrating functions. *Communications on Pure and Applied Mathematics*, 71(12):2609–2647, 2018.